

Insights into the pH-dependent Behavior of N-Doped Carbons for the Oxygen Reduction Reaction by First-Principles Calculations

Mingpeng Chen, Yuan Ping,* Yat Li,* and Tao Cheng*



Cite This: *J. Phys. Chem. C* 2021, 125, 26429–26436



Read Online

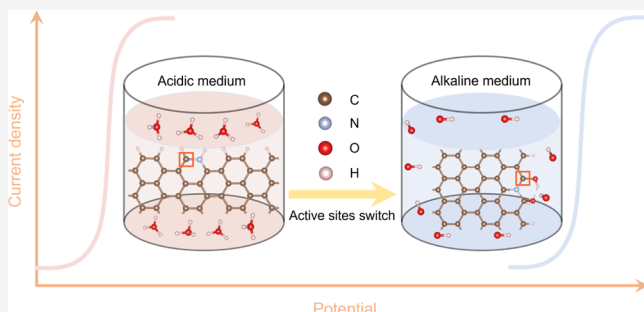
ACCESS |

Metrics & More

Article Recommendations

Supporting Information

ABSTRACT: The oxygen reduction reaction (ORR) is one of the important cathodic reactions because of its central role in important applications, such as fuel cells. Nitrogen (N)-doped carbons have been demonstrated to be one of the most promising and affordable materials as an ORR catalyst. However, their catalytic performance under acidic conditions is about two orders inferior than that under basic conditions, which is too low to be significant. Such an unexpected pH-dependent behavior has not been adequately explained and is still under debate. In this work, we investigate this pH-dependent behavior by using first-principles density functional theory (DFT) calculations. With consideration of the solvation effect and applied voltage, our simulation results show switching of active sites from pyridinic N to graphitic N that explains the changes in reaction rates from acidic to alkaline conditions. These observations not only well explain the existing experiment but also provide guidance for designing more efficient carbon-based catalysts for the ORR in an acidic medium.



1. INTRODUCTION

The oxygen reduction reaction (ORR) is the cathodic reaction of a fuel cell with a four electron-transfer process that associates with a significant energy barrier, which limits the reaction efficiency. Platinum (Pt) is one of the most efficient catalysts for the ORR in prototype fuel cell applications.^{1–9} However, the high cost and scarcity of Pt significantly limit its wide commercialization, leaving the fuel cell-driven automobiles less competitive with the electric vehicles powered by batteries. In addition, Pt-based catalysts also suffer from problems such as time-dependent drift, CO deactivation, and so forth,^{10,11} which cannot be fully addressed in the near future. Significant efforts have been carried out to search for alternative materials to replace Pt.^{12–22} Nitrogen (N)-doped carbons have been demonstrated to be one of the most promising materials because of their low cost, high abundance, and strong resistance to the poisoning of CO.^{13,23,24}

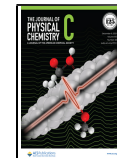
Previous studies show that the activities of N-doped carbons in acidic medium are much lower than that in alkaline medium with a ~0.2 V increase in overpotential.^{20,25–27} This lower performance under acidic conditions seriously hinders their applications in proton-exchange membrane fuel cells (PEMFCs).²⁸ To date, no unified theory can fully explain the pH-dependent behavior of N-doped carbons, leaving this important question under debate. Ramaswamy and Mukerjee proposed that the hydroxyl adsorption on N-doped carbon promotes the outer-sphere electron transfer in the ORR, which explains the experimentally observed increased activity in alkaline medium.²⁹ Another possible explanation, also

proposed by Ramaswamy and Mukerjee, attributes the pH dependence of N-doped carbon to the pH-dependent H_2O_2 stability.³⁰ As a weak acid with a $\text{p}K_a$ of 11.7, H_2O_2 undergoes sluggish disproportionation in acid because of unfavorable kinetics. Interestingly, such a disproportionation reaction significantly increases as pH increases with a maximum at pH 11–13. Wan *et al.* proposed that the pH-dependent behavior is due to the different interactions of the active sites with oxygen in different pH environments.³¹ Rojas-Carbonell *et al.* claimed that the behavior could be determined from the affinity of protons and hydroxyls toward multiple functional groups present on the surface of the N-doped carbons.³² Despite the debate, they all agree that the pH-dependent behavior is likely related to the surface structural change of N-doped carbons. Yet, it is challenging to experimentally observe the structural changes. For example, Herranz *et al.* claimed that the pH dependence of N-doped carbons is related to the protonation of pyridinic N and subsequent anion binding.³³ Nonetheless, once pyridinic N is protonated, the anion will spontaneously bind to the protonated N due to electrostatic interaction. These two processes are entangled and cannot be

Received: August 19, 2021

Revised: October 10, 2021

Published: November 29, 2021



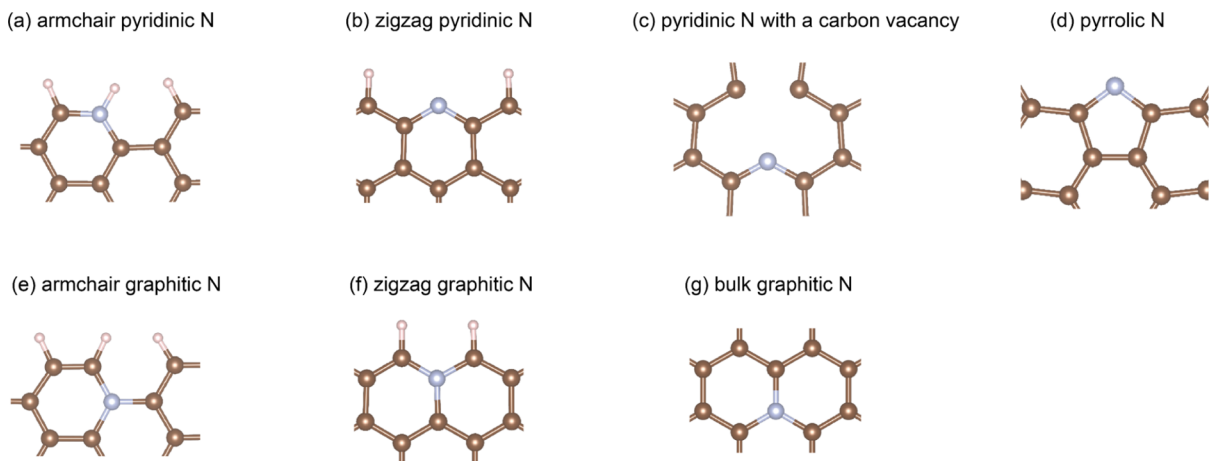


Figure 1. Possible N-doped carbon structures, including (a) armchair pyridinic N, (b) zigzag pyridinic N, (c) pyridinic N with a carbon vacancy, (d) pyrrolic N, (e) armchair graphitic N, (f) zigzag graphitic N, and (g) bulk graphitic N. Brown, pink, and silver atoms are carbon, hydrogen, and nitrogen, respectively. The color coding is the same for the rest of this paper.

separately investigated by only using experimental approaches. To tackle this question, theoretical calculations such as first-principles density functional theory (DFT) are necessary to provide an alternative approach to distinguish the role of the protonation of pyridinic N that resembles the operando experimental conditions.

One structure, such as pyridinic N alone, cannot fully explain the pH-dependent behavior of N-doped carbons. Instead, recent studies suggest that multiple possible active sites are necessary to well explain this pH-dependent behavior.^{34–37} We also notice that the assignment of the active sites is highly related to the experimental conditions. For example, in an acidic environment, pyridinic N is usually considered to be the active site.³⁸ Instead, graphitic N is confirmed to be the active site when the measurements are conducted in an alkaline environment.^{34–37} We believe that both pyridinic N and graphitic N should be taken into consideration to explain the pH-dependent behavior of N-doped carbon. Now the question is, what are the specific roles of pyridinic N and graphitic N under different pH conditions?

We hypothesize that the pH-dependent behavior is due to the switching of the active sites in different pH environments. Our calculated results verify that when the experimental condition changes from an acidic to alkaline environment, active sites gradually switch from pyridinic N to graphitic N. In an acidic environment, the protonation of pyridinic N increases its activity, while in an alkaline medium, the attachment of OH to the edge of graphitic N-doped carbon increases its activity. The trend and onset potentials of different active sites match well with the experimental values.^{26,35,38–40} Our findings deepen the understanding of the pH-dependent behavior of N-doped carbons, which is of great significance to develop more efficient carbon-based catalysts for the ORR in an acidic medium.

2. METHODS AND MODELS

2.1. Computational Methods. Vacuum density functional theory (DFT) optimizations were performed by using Quantum ESPRESSO (QE) at the level of the Perdew–Burke–Ernzerhof (PBE) exchange–correlation functional with the plane-wave basis set.^{41,42} The van der Waals dispersion correction scheme (DFT + D2) was included in the calculation to correct the long-range dispersion.⁴³ The solvation effect is

considered with the implicit solvation model of CANDLE as implemented in JDFTx that has been verified for various metallic and ionic surfaces.^{44–47} JDFTx also has the implementation of the grand canonical free energy calculation by adjusting the total number of electron transfers to match the target applied potential (U).^{48,49} ZPE and entropy correction are included to derive the free energy using phonon frequency calculations by using QE.⁵⁰ The Vienna Ab initio Simulation Package (VASP) is employed to perform transition state (TS) search. Specifically, the nudged elastic band (NEB) method is used to locate the TS, which is further refined by DIMER. Additional frequency calculation is carried out to confirm that only one imaginary frequency (saddle point) with the vibrational mode connects reactants and products. More computational details are in the Supporting Information.

2.2. Computational Models. According to the experimental analysis, different configurations of pyridinic N and graphitic N are considered as shown in Figure 1. We first benchmark the convergence of the formation energy with a different number of carbon atoms on both armchair and zigzag pyridinic N structures (Figure S1, Supporting Information). The calculation results show that the formation energies of armchair pyridinic N are always 0.15–0.20 eV lower than those of zigzag pyridinic N structures, which suggests that armchair pyridinic N is more stable. The formation energy of pyridinic N with a carbon vacancy is about 5.5 eV higher than that of armchair and zigzag pyridinic N structures. Therefore, we do not consider it in the following calculations. The convergence of armchair pyridinic N structures requires large width. Therefore, we choose 40 carbon atoms that reach the required accuracy at an affordable cost. We choose the zigzag configuration in the following calculations for graphitic N-doped carbon because it has been demonstrated that the formation energies of the zigzag configuration are the lowest among the three possible graphitic N configurations (Figure 1d–f).⁵¹ In the graphitic N-doped carbon model, the same number of 40 carbon atoms is used for consistency with the pyridinic N doping. The edges of both pyridinic N and graphitic N-doped carbon are terminated by H.⁵² The high formation energies of both pyridinic N with a carbon vacancy and bulk graphitic N (Table S1) are consistent with previous reports showing that incorporating N into the edges of carbon matrixes is much easier than into the bulk/interior.^{53–55}

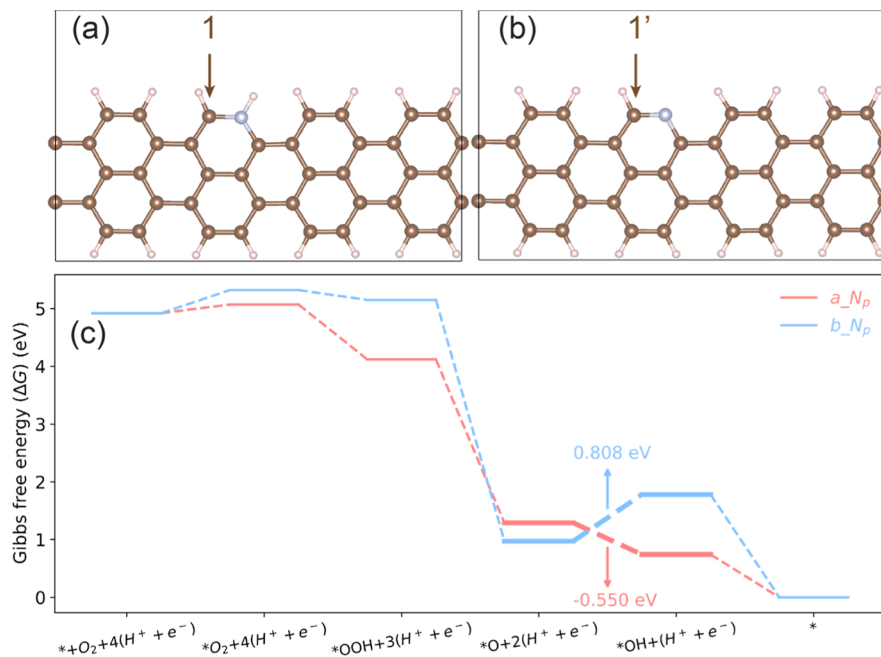


Figure 2. Structures of pyridinic N-doped carbon and the related ORR reaction pathway. (a) Protonated pyridinic N-doped carbon (a_N_p) structure. (b) Deprotonated pyridinic N-doped carbon (b_N_p) structure. (c) Gibbs free energy profiles of the ORR on a_N_p (in red) and b_N_p (in blue) surfaces. The Gibbs free energy changes of PDSs (bold lines) are labeled.

3. RESULTS AND DISCUSSION

3.1. Pyridinic N. Pyridinic N is a weak base with a pK_a around 5.3³³ and is protonated under experimental acidic conditions. The structure is denoted as a_N_p . Instead, deprotonated pyridinic N-doped carbon is used to simulate the structure in an alkaline medium, which is denoted as b_N_p . The two structures are shown in Figure 2a,b, respectively. ORR reaction pathways for both structures are computed by investigating the elementary reactions (Figure 2c). The detailed numbers of the ORR reaction pathway and the optimized geometries of reactive intermediates can be found in Table S2 and Figures S2, S3 (Supporting Information), respectively. The DFT calculations show that the reconstructions of the O-adsorbed surface (Figure S4, Supporting Information) dramatically lower the energy of the *O state, which makes the third protonation step ($^*O + H^+ + e^- = ^*OH$) of a_N_p and b_N_p become the potential determining step (PDS). During our calculations, an implicit solvation model of CANDLE is used to simulate the interaction between solvent and a catalyst. In order to verify the validity of the implicit solvation model, an additional calculation with an explicit water molecule flowing on the surface of a_N_p is computed for the elementary step: $^*OH + H^+ + e^- = ^*H_2O$. It is found that there is no significant change in ΔG between the two cases (Figure S5), suggesting that the implicit solvation model employed here is reliable.

The first proton-coupled electron transfer (PCET) step ($^*O_2 + H^+ + e^- = ^*OOH$) of b_N_p is endothermic with a free energy change of 0.398 eV (Table S2, Supporting Information), indicating that the adsorption of O_2 on the surface is weak. Compared to b_N_p , the O_2 adsorption is stronger on a_N_p . Projected density of states (PDOS) is calculated to understand the improved O_2 adsorption on a_N_p . As shown in Figure 3a (PDOS of both a_N_p and b_N_p surfaces), the electron distribution is enhanced around the Fermi level for a_N_p compared to b_N_p . The PDOS of the carbon adjacent to

the N dopant (carbon #1 for a_N_p and #1' for b_N_p) is also computed and compared in Figure 3b. The results show that the PDOS at Fermi level of carbon #1 in a_N_p is still much higher than that of carbon #1' in b_N_p , indicating that carbon #1 has more available states for the charge transfer with the adsorbates. The electron density mappings of both structures also reach the same conclusion (Figure 3c,d), consistent with the PDOS analysis. The charge density difference for a_N_p before and after protonation in Figure S6 directly shows the electron density enrichment on carbon #1 in the protonation process. Bader charge analysis is employed to quantitatively compare the electron density on carbon #1 and #1' as well.⁴⁸ The equation to compute the Bader charge is defined as below⁵⁴

$$\Delta Q = Q(\text{N doped carbon}) - Q(\text{non-N doped carbon}) \quad (1)$$

where $Q(\text{N-doped carbon})$ is the charge (electrons) on carbon #1 (#1') in the N-doped carbon structure while $Q(\text{non-N-doped carbon})$ is the charge (electrons) on the corresponding carbon in non-N-doped carbon nanoribbon. Larger ΔQ indicates more electrons being transferred to the carbon site. Thus, the less negative ΔQ value of carbon #1 (-1.01) in a_N_p compared to carbon #1' (-1.43) in b_N_p suggests higher electron density on carbon #1, which is consistent with PDOS, electron density mapping, and charge density difference results. A higher electron density of carbon #1 (#1') is desirable to facilitate the formation of a new C–O bond. In addition, we carefully analyzed the molecular orbital change before and after the protonation of pyridinic N (Figure S6). Before the protonation of pyridinic N, the hybridization of the two antibonding π^* electrons from O_2 molecules with the three π_x , π_y electrons in the bonding orbital of NC will generate one electron in the antibonding π_x^* orbital (Figure S7a). However, after the protonation of pyridinic N, the molecular orbital after hybridization will not generate electrons distributing in the

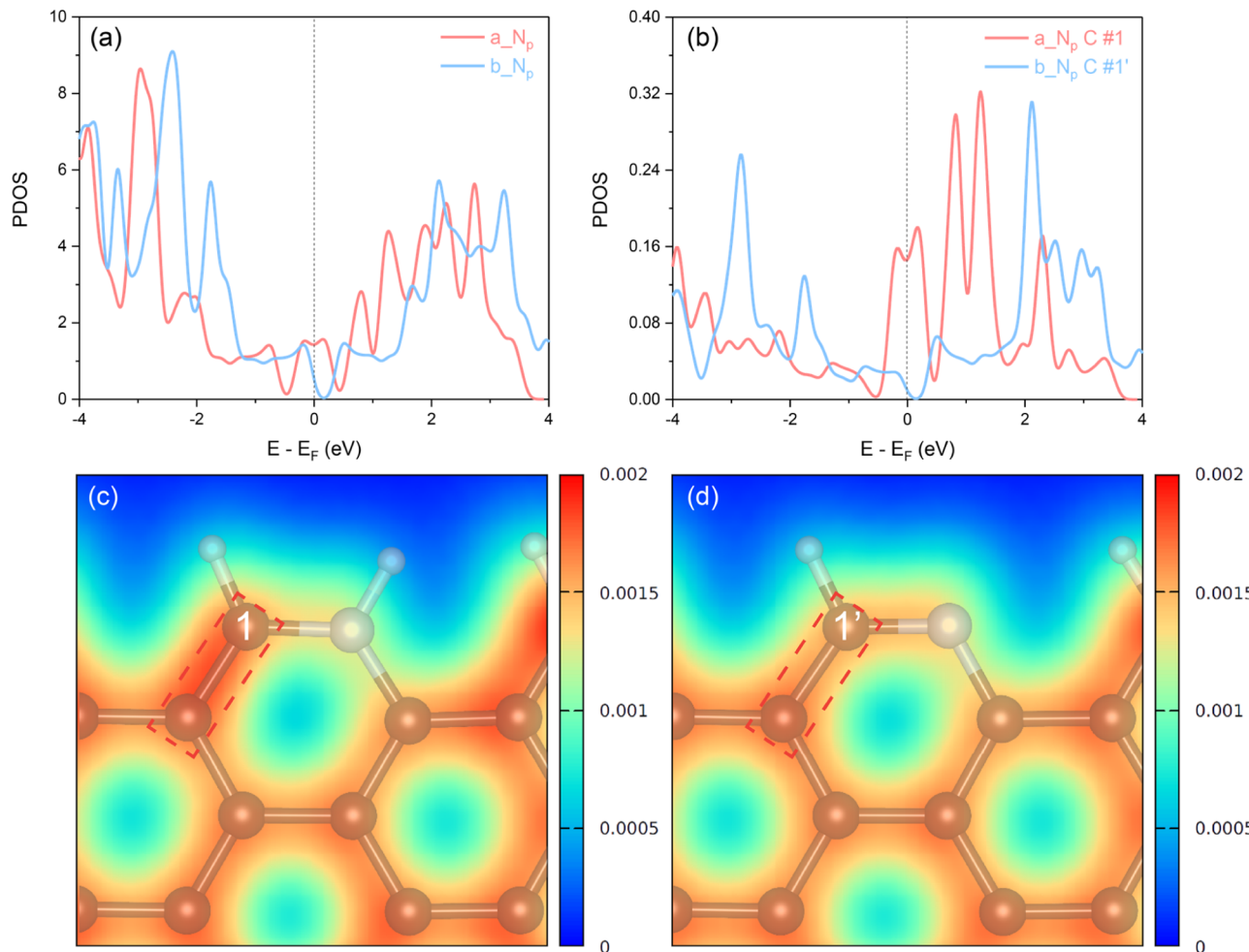


Figure 3. Electronic structures of a_N_p and b_N_p . (a) PDOS of the whole a_N_p and b_N_p structures. (b) PDOS of only carbon #1 in a_N_p and #1' in b_N_p . The electron density mappings of (c) a_N_p and (d) b_N_p partial structures. The red frames in (c,d) are highlighting the increased electron density on carbon #1.

antibonding orbitals anymore (Figure S7b), which makes the O_2 adsorption or the electron transfer between N-doped carbon and oxygen species easier, as shown in Figure 2c.

3.2. Graphitic N. Graphitic N is employed to simulate the ORR in an acidic environment (Figure 4a, denoted as N_g) because the bare graphitic N has been demonstrated to be stable in acidic medium.³² In alkaline solution, graphene is prone to be oxidized, and the reasonable graphitic N should have OH attached to the edge for simulation in an alkaline medium (Figure 4b, denoted as $N_g + 2OH$). Two OH attaching to the edge corresponds to an oxygen concentration of ~5%, which is consistent with experimental evidence showing that the as-synthesized N-doped carbon is oxidized with 5% O.^{56–58} The ORR reaction pathways on both structures are calculated and compared in Figure 4c. The detailed numbers and structures of intermediates are listed in Table S2 and Figures S8, S9 (Supporting Information). The *OOH adsorption geometry on the bare N_g surface is different from that on the pyridinic N-doped carbon surface. Instead of taking an end-on adsorption configuration, *OOH breaks into *H and *OH and adsorbs on the surface in a side-on configuration with the third protonation step ($*O + H^+ + e^- = *OH$) as the PDS, which determines an onset potential of 0.492 V. Due to the steric effect (as shown in Figure S10, Supporting Information), *OOH adsorption on the $N_g + 2OH$

surface is much weaker compared to the bare N_g surface and goes back to the end-on adsorption configuration (Figure S9, Supporting Information). This changes the PDS to the desorption of OH with an onset potential of 0.693 V.

3.3. Potential Dependence of the Structural Evolution of N-Doped Carbon. In order to confirm that the structural changes do occur under working conditions, we calculate the potential dependence of the Gibbs free energy changes of these processes at given pH. The protonation of pyridinic N (Figure 5a) is simulated at pH = 1, corresponding to an acidic environment. An alkaline pH = 13 is used to simulate the OH attachment to the edge of graphitic N (Figure 5b). Detailed equations and numbers are listed in Supporting Information. The slope of the protonation of pyridinic N in Figure 5a is positive. Instead, the slope of the OH attachment is negative in Figure 5b. This opposite trend is because the former is a reduction process while the latter is an oxidation reaction. Under working conditions ($U_{RHE} < 1$ V), the Gibbs free energy (ΔG) of these two processes is negative, indicating the spontaneous protonation of pyridinic N and OH attachment to the edge of graphitic N.

3.4. Kinetics of the ORR Reaction Pathway. We also consider the kinetics of the ORR pathway in this work. The TS structures from DIMER calculations are shown in Figure 6. All the TS structures are confirmed with only one imaginary

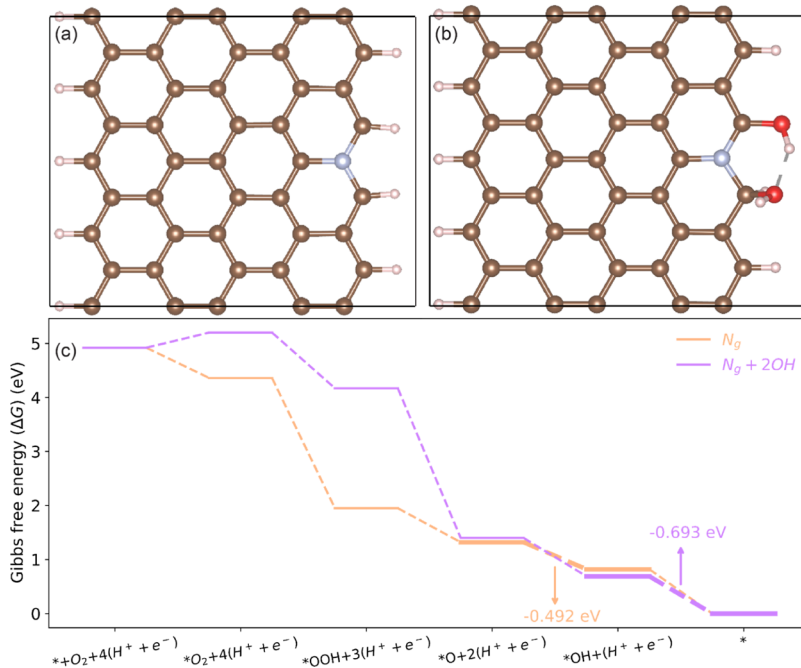


Figure 4. Structures of the graphitic N-doped carbon surface and related ORR reaction pathways. Structures of (a) bare graphitic N-doped carbon (N_g) and (b) 2OH-adsorbed graphitic N-doped carbon ($N_g + 2OH$). (c) Gibbs free energy profiles of the ORR on N_g (orange) and $N_g + 2OH$ (purple) structures. The Gibbs free energy changes of PDSs (bold lines) are labeled.

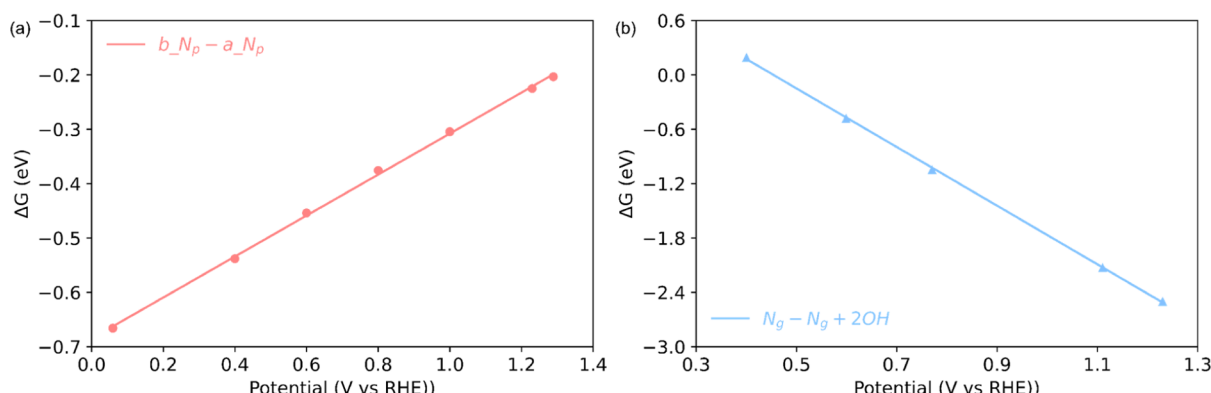


Figure 5. Potential dependence of the Gibbs free energy changes of the structural evolution of N-doped carbon. (a) Protonation of pyridinic N at pH = 1 and (b) OH attachment to the edge of graphitic N at pH = 13.

frequency, which connects the reactants and products. On a_N_p surface, the free energy barrier of $* \rightarrow *OOH$ is 0.493 eV while the PDS ($*OH \rightarrow *$) of the $N_g + 2OH$ surface has an energy barrier of 0.360 eV. More details of free energy barrier calculation results are provided in Supporting Information. The lower energy barrier of the $N_g + 2OH$ surface indicates that kinetically it is also more favorable for the ORR to proceed on the $N_g + 2OH$ surface than on the a_N_p surface. The bond length analysis of the $N_g + 2OH$ initial state (IS) and TS shows that there is no big difference between the 1–2 (1'–2'), 2–3 (2'–3'), and 3–4 (3'–4') distance, while the distance between 3 and 5 significantly decreases from 2.50 to 1.47 Å. These structural features of the TS suggest that the H-bond interaction between the attached OH and adsorbed H_2O molecule could help lower the energy barrier of the ORR on the $N_g + 2OH$ surface.

3.5. Comparison of Pyridinic N with Graphitic N. The comparison of the predicted catalytic performance of the four active sites is shown in Scheme 1. The comparison reveals

switching of active sites at different pH values. Pyridinic N is more active in acidic medium because a_N_p has a higher onset potential (0.550 V) than that of the N_g surface (0.492 V). The predicted onset potential of 0.550 V is close to the experimentally measured onset potential of ~0.5 V using 2.5% N-doped carbon (the same doping concentration is used in our simulation unit cell).³⁸ Under alkaline conditions, a higher onset potential of 0.693 V of $N_g + 2OH$ indicates that OH-attached edges of graphitic N are the active sites in alkaline medium, consistent with literature observation.^{34–37} The calculation also reveals that $N_g + 2OH$ has a higher onset potential than a_N_p , which agrees well with the strong pH-dependent behavior of N-doped carbon observed experimentally.^{25–27}

4. CONCLUSIONS

In summary, we have investigated the strong pH-dependent behavior of N-doped carbon for the ORR with DFT simulations. The simulation results show that the pH-

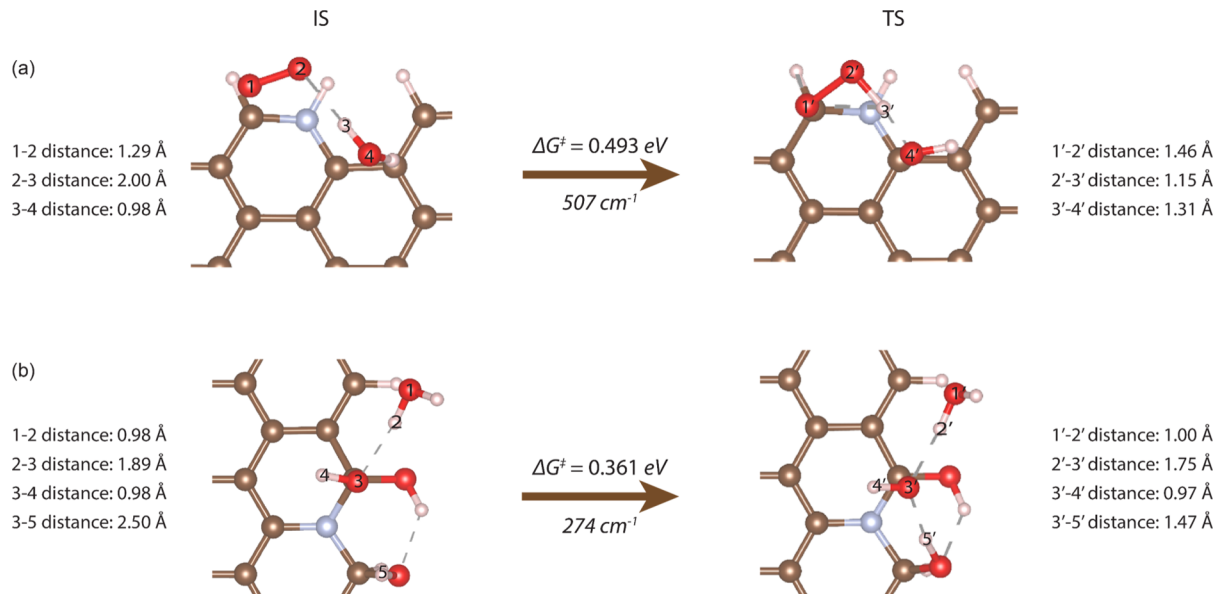
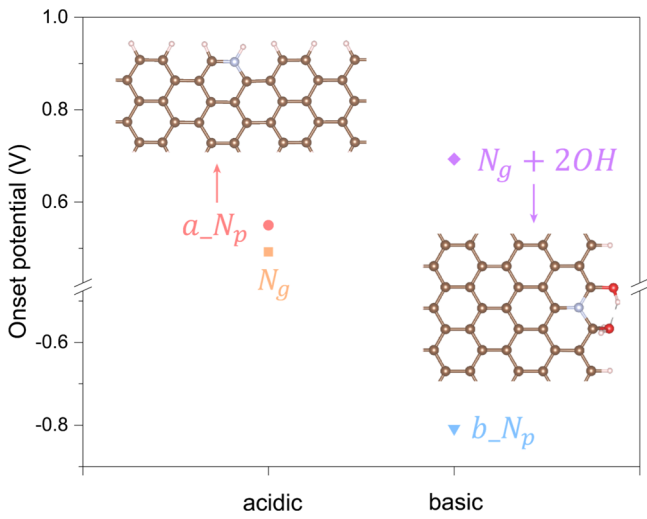


Figure 6. Energy barrier calculation results. Energy barriers, imaginary frequencies, and corresponding bond length changes of (a) a_{N_p} surface ($* \rightarrow *_{\text{OOH}}$) and (b) $N_g + 2\text{OH}$ surface ($*_{\text{OH}} \rightarrow *$).

Scheme 1. Activity Comparison of Different Active Sites in Acidic and Alkaline Medium



dependent performance can be explained as the switching of the active sites, specifically from pyridinic N in an acidic medium to graphitic N under basic conditions. In acidic electrolyte, protonated pyridinic N is predicted to be the active site with an onset potential of 0.550 V. In contrast, OH-attached edges of the graphitic N-doped surface is predicted to be the active sites in alkaline electrolyte, with an onset potential of 0.693 V. These predictions not only reproduce the intriguing experimental observations that N-doped carbon is more active in the alkaline medium than that in acidic medium with a ~ 0.2 V onset potential increase but also elucidate the roles of pyridinic N and graphitic N under different pH conditions. More importantly, our results also suggest two possible ways to enhance the activity of N-doped carbons for the ORR in an acidic medium: (a) increase the number of active sites, that is, increase the concentration of pyridinic N, which has been verified experimentally and³⁸ (b) increase the intrinsic activity of active sites, for example, functionalize the

graphitic N-doped carbon surface with suitable functional groups that are stable in acidic medium to boost the activity. These findings provide new principles for designing more efficient carbon-based materials for the ORR in the acidic medium.

ASSOCIATED CONTENT

Supporting Information

The Supporting Information is available free of charge at <https://pubs.acs.org/doi/10.1021/acs.jpcc.1c07362>.

Details of computational methods and structural models, intermediates in the ORR reaction pathway of four active sites, explicit solvation model test, charge density difference calculation, molecular orbital analysis, and the data of the ORR reaction pathway of the four active sites (PDF).

AUTHOR INFORMATION

Corresponding Authors

Yuan Ping – Department of Chemistry and Biochemistry, University of California, Santa Cruz, California 95064, United States; orcid.org/0000-0002-0123-3389; Email: yuanping@ucsc.edu

Yat Li – Department of Chemistry and Biochemistry, University of California, Santa Cruz, California 95064, United States; orcid.org/0000-0002-8058-2084; Email: yatli@ucsc.edu

Tao Cheng – Institute of Functional Nano & Soft Materials (FUNSOM), Jiangsu Key Laboratory for Carbon-Based Functional Materials & Devices, Joint International Research Laboratory of Carbon-Based Functional Materials and Devices, Soochow University, Suzhou, Jiangsu 215123, China; orcid.org/0000-0003-4830-177X; Email: tcheng@suda.edu.cn

Author

Mingpeng Chen – Department of Chemistry and Biochemistry, University of California, Santa Cruz, California 95064, United States

Complete contact information is available at:
<https://pubs.acs.org/10.1021/acs.jpcc.1c07362>

Notes

The authors declare no competing financial interest.

ACKNOWLEDGMENTS

Y.L. acknowledges the financial support by the Merced nAnomaterials Center for Energy and Sensing (MACES), a NASA-funded MIRO center, under award NNX15AQ01A. Y.P. acknowledges the financial support by the National Science Foundation under grant number #CHE-1904547. T.C. thanks the National Natural Science Foundation of China (21903058 and 22003044), the Natural Science Foundation of Jiangsu Higher Education Institutions (SBK20190810), the Jiangsu Province High-Level Talents (JNHB-106), the Priority Academic Program Development of Jiangsu Higher Education Institutions (PAPD), Collaborative Innovation Center of Suzhou Nano Science & Technology for financial support. M.C. thanks Yiming Lu for the helpful discussion. This research used resources of the Scientific Data and Computing center, a component of the Computational Science Initiative, at Brookhaven National Laboratory under Contract No. DESC0012704, the lux supercomputer at UC Santa Cruz, funded by NSF MRI grant AST 1828315, the Extreme Science and Engineering Discovery Environment (XSEDE) which is supported by National Science Foundation Grant No. ACI-1548562.

REFERENCES

- (1) Li, M.; Zhao, Z.; Cheng, T.; Fortunelli, A.; Chen, C.-Y.; Yu, R.; Zhang, Q.; Gu, L.; Merinov, B. V.; Lin, Z.; et al. Ultrafine Jagged Platinum Nanowires Enable Ultrahigh Mass Activity for the Oxygen Reduction Reaction. *Science* **2016**, *354*, 1414.
- (2) Chong, L.; Wen, J.; Kubal, J.; Sen, F. G.; Zou, J.; Greeley, J.; Chan, M.; Barkholtz, H.; Ding, W.; Liu, D.-J. Ultralow-loading Platinum-cobalt Fuel Cell Catalysts Derived from Imidazolate Frameworks. *Science* **2018**, *362*, 1276.
- (3) Chen, C.; Kang, Y.; Huo, Z.; Zhu, Z.; Huang, W.; Xin, H. L.; Snyder, J. D.; Li, D.; Herron, J. A.; Mavrikakis, M.; et al. Highly Crystalline Multimetallic Nanoframes with Three-Dimensional Electrocatalytic Surfaces. *Science* **2014**, *343*, 1339.
- (4) Tian, X.; Zhao, X.; Su, Y.-Q.; Wang, L.; Wang, H.; Dang, D.; Chi, B.; Liu, H.; Hensen, E. J. M.; Lou, X. W.; et al. Engineering Bunched Pt-Ni Alloy Nanocages for Efficient Oxygen Reduction in Practical Fuel Cells. *Science* **2019**, *366*, 850.
- (5) Bu, L.; Zhang, N.; Guo, S.; Zhang, X.; Li, J.; Yao, J.; Wu, T.; Lu, G.; Ma, J.-Y.; Su, D.; et al. Biaxially Strained PtPb/Pt Core/shell Nanoplate Boosts Oxygen Reduction Catalysis. *Science* **2016**, *354*, 1410.
- (6) Huang, X.; Zhao, Z.; Cao, L.; Chen, Y.; Zhu, E.; Lin, Z.; Li, M.; Yan, A.; Zettl, A.; Wang, Y. M.; et al. High-performance Transition Metal-doped Pt₃Ni Octahedra for Oxygen Reduction Reaction. *Science* **2015**, *348*, 1230.
- (7) Luo, M.; Zhao, Z.; Zhang, Y.; Sun, Y.; Xing, Y.; Lv, F.; Yang, Y.; Zhang, X.; Hwang, S.; Qin, Y.; et al. PdMo Bimetallene for Oxygen Reduction Catalysis. *Nature* **2019**, *574*, 81–85.
- (8) Chen, Y.; Cheng, T.; Goddard, W. A. III Atomistic Explanation of the Dramatically Improved Oxygen Reduction Reaction of Jagged Platinum Nanowires, 50 Times Better than Pt. *J. Am. Chem. Soc.* **2020**, *142*, 8625–8632.
- (9) Greeley, J.; Stephens, I. E. L.; Bondarenko, A. S.; Johansson, T. P.; Hansen, H. A.; Jaramillo, T. F.; Rossmeisl, J.; Chorkendorff, I.; Nørskov, J. K. Alloys of Platinum and Early Transition Metals as Oxygen Reduction Electrocatalysts. *Nat. Chem.* **2009**, *1*, 552–556.
- (10) Dai, L.; Xue, Y.; Qu, L.; Choi, H.-J.; Baek, J.-B. Metal-Free Catalysts for Oxygen Reduction Reaction. *Chem. Rev.* **2015**, *115*, 4823–4892.
- (11) Liu, X.; Dai, L. Carbon-based Metal-free Catalysts. *Nat. Rev. Mater.* **2016**, *1*, 16064.
- (12) Zitolo, A.; Goellner, V.; Armel, V.; Sougrati, M.-T.; Mineva, T.; Stievano, L.; Fonda, E.; Jaouen, F. Identification of Catalytic Sites for Oxygen Reduction in Iron- and Nitrogen-doped Graphene Materials. *Nat. Mater.* **2015**, *14*, 937–942.
- (13) Gong, K.; Du, F.; Xia, Z.; Durstock, M.; Dai, L. Nitrogen-Doped Carbon Nanotube Arrays with High Electrocatalytic Activity for Oxygen Reduction. *Science* **2009**, *323*, 760.
- (14) Yuan, Y.; Wang, J.; Adimi, S.; Shen, H.; Thomas, T.; Ma, R.; Attfield, J. P.; Yang, M. Zirconium Nitride Catalysts Surpass Platinum for Oxygen Reduction. *Nat. Mater.* **2020**, *19*, 282–286.
- (15) Lim, K. R. G.; Handoko, A. D.; Nemanic, S. K.; Wyatt, B.; Jiang, H.-Y.; Tang, J.; Anasori, B.; Seh, Z. W. Rational Design of Two-Dimensional Transition Metal Carbide/Nitride (MXene) Hybrids and Nanocomposites for Catalytic Energy Storage and Conversion. *ACS Nano* **2020**, *14*, 10834–10864.
- (16) Eom, C. J.; Kuo, D.-Y.; Adamo, C.; Moon, E. J.; May, S. J.; Crumlin, E. J.; Schlom, D. G.; Suntivich, J. Tailoring Manganese Oxide with Atomic Precision to Increase Surface Site Availability for Oxygen Reduction Catalysis. *Nat. Commun.* **2018**, *9*, 4034.
- (17) Mu, C.; Mao, J.; Guo, J.; Guo, Q.; Li, Z.; Qin, W.; Hu, Z.; Davey, K.; Ling, T.; Qiao, S. Z. Rational Design of Spinel Cobalt Vanadate Oxide Co₂VO₄ for Superior Electrocatalysis. *Adv. Mater.* **2020**, *32*, 1907168.
- (18) Liu, T.; Kou, T.; Bulmahn, D.; Ortuno-Quintana, C.; Liu, G.; Lu, J. Q.; Li, Y. Tuning the Electrochemical Properties of Nitrogen-Doped Carbon Aerogels in a Blend of Ammonia and Nitrogen Gases. *ACS Appl. Energy Mater.* **2018**, *1*, 5043–5053.
- (19) Kulkarni, A.; Siahrostami, S.; Patel, A.; Nørskov, J. K. Understanding Catalytic Activity Trends in the Oxygen Reduction Reaction. *Chem. Rev.* **2018**, *118*, 2302–2312.
- (20) Qian, Y.; Liu, Q.; Sarnello, E.; Tang, C.; Chng, M.; Shui, J.; Li, T.; Pennycook, S. J.; Han, M.; Zhao, D. MOF-Derived Carbon Networks with Atomically Dispersed Fe–N_x Sites for Oxygen Reduction Reaction Catalysis in Acidic Media. *ACS Mater. Lett.* **2019**, *1*, 37–43.
- (21) Yan, Y.; Zhao, Z.; Zhao, J.; Xu, Y.; Xu, Y.; Zhao, Y.; Tang, W.; Lee, J.-M. Ultrathin CuNi Nanosheets for CO₂ Reduction and O₂ Reduction Reaction in Fuel Cells. *ACS Mater. Lett.* **2021**, *3*, 1143–1150.
- (22) Chen, P.; Zhang, N.; Zhou, T.; Tong, Y.; Yan, W.; Chu, W.; Wu, C.; Xie, Y. Tailoring Electronic Structure of Atomically Dispersed Metal–N₃S₁ Active Sites for Highly Efficient Oxygen Reduction Catalysis. *ACS Mater. Lett.* **2019**, *1*, 139–146.
- (23) Liang, J.; Jiao, Y.; Jaroniec, M.; Qiao, S. Z. Sulfur and Nitrogen Dual-Doped Mesoporous Graphene Electrocatalyst for Oxygen Reduction with Synergistically Enhanced Performance. *Angew. Chem., Int. Ed.* **2012**, *51*, 11496–11500.
- (24) Jiao, Y.; Zheng, Y.; Jaroniec, M.; Qiao, S. Z. Design of Electrocatalysts for Oxygen- and Hydrogen-involving Energy Conversion Reactions. *Chem. Soc. Rev.* **2015**, *44*, 2060–2086.
- (25) Lee, S. H.; Kim, J.; Chung, D. Y.; Yoo, J. M.; Lee, H. S.; Kim, M. J.; Mun, B. S.; Kwon, S. G.; Sung, Y.-E.; Hyeon, T. Design Principle of Fe–N–C Electrocatalysts: How to Optimize Multimodal Porous Structures? *J. Am. Chem. Soc.* **2019**, *141*, 2035–2045.
- (26) Li, D.; Jia, Y.; Chang, G.; Chen, J.; Liu, H.; Wang, J.; Hu, Y.; Xia, Y.; Yang, D.; Yao, X. A Defect-Driven Metal-free Electrocatalyst for Oxygen Reduction in Acidic Electrolyte. *Chem* **2018**, *4*, 2345–2356.
- (27) Ramaswamy, N.; Tylus, U.; Jia, Q.; Mukerjee, S. Activity Descriptor Identification for Oxygen Reduction on Nonprecious Electrocatalysts: Linking Surface Science to Coordination Chemistry. *J. Am. Chem. Soc.* **2013**, *135*, 15443–15449.
- (28) Zhao, Z.; Hossain, M. D.; Xu, C.; Lu, Z.; Liu, Y.-S.; Hsieh, S.-H.; Lee, I.; Gao, W.; Yang, J.; Merinov, B. V.; et al. Tailoring a Three-

- Phase Microenvironment for High-Performance Oxygen Reduction Reaction in Proton Exchange Membrane Fuel Cells. *Matter* **2020**, *3*, 1774–1790.
- (29) Ramaswamy, N.; Mukerjee, S. Influence of Inner- and Outer-Sphere Electron Transfer Mechanisms during Electrocatalysis of Oxygen Reduction in Alkaline Media. *J. Phys. Chem. C* **2011**, *115*, 18015–18026.
- (30) Ramaswamy, N.; Mukerjee, S. Alkaline Anion-Exchange Membrane Fuel Cells: Challenges in Electrocatalysis and Interfacial Charge Transfer. *Chem. Rev.* **2019**, *119*, 11945–11979.
- (31) Wan, K.; Yu, Z.-p.; Li, X.-h.; Liu, M.-y.; Yang, G.; Piao, J.-h.; Liang, Z.-x. pH Effect on Electrochemistry of Nitrogen-Doped Carbon Catalyst for Oxygen Reduction Reaction. *ACS Catal.* **2015**, *5*, 4325–4332.
- (32) Rojas-Carbonell, S.; Artyushkova, K.; Serov, A.; Santoro, C.; Matanovic, I.; Atanassov, P. Effect of pH on the Activity of Platinum Group Metal-Free Catalysts in Oxygen Reduction Reaction. *ACS Catal.* **2018**, *8*, 3041–3053.
- (33) Herranz, J.; Jaouen, F.; Lefèvre, M.; Kramm, U. I.; Proietti, E.; Dodelet, J.-P.; Bogdanoff, P.; Fiechter, S.; Abs-Wurmbach, I.; Bertrand, P.; et al. Unveiling N-Protonation and Anion-Binding Effects on Fe/N/C Catalysts for O₂ Reduction in Proton-Exchange-Membrane Fuel Cells. *J. Phys. Chem. C* **2011**, *115*, 16087–16097.
- (34) Xu, Z.; Zhou, Z.; Li, B.; Wang, G.; Leu, P. W. Identification of Efficient Active Sites in Nitrogen-Doped Carbon Nanotubes for Oxygen Reduction Reaction. *J. Phys. Chem. C* **2020**, *124*, 8689–8696.
- (35) Wang, N.; Lu, B.; Li, L.; Niu, W.; Tang, Z.; Kang, X.; Chen, S. Graphitic Nitrogen Is Responsible for Oxygen Electroreduction on Nitrogen-Doped Carbons in Alkaline Electrolytes: Insights from Activity Attenuation Studies and Theoretical Calculations. *ACS Catal.* **2018**, *8*, 6827–6836.
- (36) Sharifi, T.; Hu, G.; Jia, X.; Wågberg, T. Formation of Active Sites for Oxygen Reduction Reactions by Transformation of Nitrogen Functionalities in Nitrogen-Doped Carbon Nanotubes. *ACS Nano* **2012**, *6*, 8904–8912.
- (37) Yang, H. B.; Miao, J.; Hung, S.-F.; Chen, J.; Tao, H. B.; Wang, X.; Zhang, L.; Chen, R.; Gao, J.; Chen, H. M.; et al. Identification of Catalytic Sites for Oxygen Reduction and Oxygen Evolution in N-doped Graphene Materials: Development of Highly Efficient Metal-free Bifunctional Electrocatalyst. *Sci. Adv.* **2016**, *2*, No. e1501122.
- (38) Guo, D.; Shibuya, R.; Akiba, C.; Saji, S.; Kondo, T.; Nakamura, J. Active Sites of Nitrogen-doped Carbon Materials for Oxygen Reduction Reaction Clarified Using Model Catalysts. *Science* **2016**, *351*, 361.
- (39) Shui, J.; Wang, M.; Du, F.; Dai, L. N-doped Carbon Nanomaterials Are Durable Catalysts for Oxygen Reduction Reaction in Acidic Fuel Cells. *Sci. Adv.* **2015**, *1*, 1400129.
- (40) Qu, L.; Liu, Y.; Baek, J.-B.; Dai, L. Nitrogen-Doped Graphene as Efficient Metal-Free Electrocatalyst for Oxygen Reduction in Fuel Cells. *ACS Nano* **2010**, *4*, 1321–1326.
- (41) Giannozzi, P.; Baroni, S.; Bonini, N.; Calandra, M.; Car, R.; Cavazzoni, C.; Ceresoli, D.; Chiarotti, G. L.; Cococcioni, M.; Dabo, I.; et al. QUANTUM ESPRESSO: a Modular and Open-source Software Project for Quantum Simulations of Materials. *J. Phys. Condens. Matter* **2009**, *21*, 395502.
- (42) Perdew, J. P.; Burke, K.; Ernzerhof, M. Generalized Gradient Approximation Made Simple. *Phys. Rev. Lett.* **1996**, *77*, 3865–3868.
- (43) Grimme, S. Semiempirical GGA-type Density Functional Constructed with a Long-range Dispersion Correction. *J. Comput. Chem.* **2006**, *27*, 1787–1799.
- (44) Sundararaman, R.; Letchworth-Weaver, K.; Schwarz, K. A.; Gunceler, D.; Ozhabes, Y.; Arias, T. A. JDFTx: Software for Joint Density-functional Theory. *SoftwareX* **2017**, *6*, 278–284.
- (45) Sundararaman, R.; Ping, Y. First-principles Electrostatic Potentials for Reliable Alignment at Interfaces and Defects. *J. Chem. Phys.* **2017**, *146*, 104109.
- (46) Chen, M.; Smart, T. J.; Wang, S.; Kou, T.; Lin, D.; Ping, Y.; Li, Y. The Coupling of Experiments with Density Functional Theory in the Electrochemical Hydrogen Evolution Reaction Studies. *J. Mater. Chem. A* **2020**, *8*, 8783–8812.
- (47) Kou, T.; Chen, M.; Wu, F.; Smart, T. J.; Wang, S.; Wu, Y.; Zhang, Y.; Li, S.; Lall, S.; Zhang, Z.; et al. Carbon Doping Switching on the Hydrogen Adsorption Activity of NiO for Hydrogen Evolution Reaction. *Nat. Commun.* **2020**, *11*, 590.
- (48) Chai, G.-L.; Hou, Z.; Shu, D.-J.; Ikeda, T.; Terakura, K. Active Sites and Mechanisms for Oxygen Reduction Reaction on Nitrogen-Doped Carbon Alloy Catalysts: Stone–Wales Defect and Curvature Effect. *J. Am. Chem. Soc.* **2014**, *136*, 13629–13640.
- (49) Duan, Z.; Henkelman, G. Identification of Active Sites of Pure and Nitrogen-Doped Carbon Materials for Oxygen Reduction Reaction Using Constant-Potential Calculations. *J. Phys. Chem. C* **2020**, *124*, 12016–12023.
- (50) Biddinger, E. J.; Ozkan, U. S. Role of Graphitic Edge Plane Exposure in Carbon Nanostructures for Oxygen Reduction Reaction. *J. Phys. Chem. C* **2010**, *114*, 15306–15314.
- (51) Tang, C.; Zhang, Q. Nanocarbon for Oxygen Reduction Electrocatalysis: Dopants, Edges, and Defects. *Adv. Mater.* **2017**, *29*, 1604103.
- (52) Lv, Q.; Si, W.; He, J.; Sun, L.; Zhang, C.; Wang, N.; Yang, Z.; Li, X.; Wang, X.; Deng, W.; et al. Selectively Nitrogen-doped Carbon Materials as Superior Metal-free Catalysts for Oxygen Reduction. *Nat. Commun.* **2018**, *9*, 3376.
- (53) Yu, M.; Trinkle, D. R. Accurate and Efficient Algorithm for Bader Charge Integration. *J. Chem. Phys.* **2011**, *134*, 064111.
- (54) Mamtani, K.; Jain, D.; Dogu, D.; Gustin, V.; Gunduz, S.; Co, A. C.; Ozkan, U. S. Insights into Oxygen Reduction Reaction (ORR) and Oxygen Evolution Reaction (OER) Active Sites for Nitrogen-doped Carbon Nanostructures (CN_x) in Acidic Media. *Appl. Catal., B* **2018**, *220*, 88–97.
- (55) Buan, M. E. M.; Cognigni, A.; Walmsley, J. C.; Muthuswamy, N.; Rønning, M. Active Sites for the Oxygen Reduction Reaction in Nitrogen-doped Carbon Nanofibers. *Catal. Today* **2020**, *357*, 248–258.
- (56) Chen, Z.; Higgins, D.; Tao, H.; Hsu, R. S.; Chen, Z. Highly Active Nitrogen-Doped Carbon Nanotubes for Oxygen Reduction Reaction in Fuel Cell Applications. *J. Phys. Chem. C* **2009**, *113*, 21008–21013.
- (57) Mamtani, K.; Jain, D.; Dogu, D.; Gustin, V.; Gunduz, S.; Co, A. C.; Ozkan, U. S. Insights into Oxygen Reduction Reaction (ORR) and Oxygen Evolution Reaction (OER) Active Sites for Nitrogen-doped Carbon Nanostructures (CN_x) in Acidic Media. *Appl. Catal. B* **2018**, *220*, 88–97.
- (58) Buan, M. E. M.; Cognigni, A.; Walmsley, J. C.; Muthuswamy, N.; Rønning, M. Active Sites for the Oxygen Reduction Reaction in Nitrogen-doped Carbon Nanofibers. *Catal. Today* **2020**, *357*, 248–258.